MRC/ABQ-R-741
Copy 282

(2)

Mission Research Corporation

IFR TRANSPORT IN RECIRCULATING ACCELERATORS

Final Report

B. B. Godfrey
B. S. Newberger
L. A. Wright
M. M. Campbell

November 1985

Prepared for: SANDIA NATIONAL LABORATORIES
Pulse Power Directorate
Post Office Box 5800
Albuquerque, NM 87185

Under: Sandia Contract 51-4447

Prepared by: MISSION RESEARCH CORPORATION
1720 Randolph Road, SE.
Albuquerque, NM 87106-4245

CONTENTS

CONTENTS (Concluded)

ILLUSTRATIONS

I. INTRODUCTION

1. BACKGROUND

Charged particle beam weapon research performed by Mission Research Corporation (MRC) for Sandia National Laboatories (SNL) during FY85 has focused on predictions of RADLAC beam propagation in the atmosphere, analysis of RADLAC beam transport in low density ionized (IFR) channels, and preliminary studies of generic IFR transport in recirculating high current electron beam inductive accelerators. This report summarizes our recirculating accelerator findings. In addition, a patent disclosure for creating IFR channels with low power electron beams has been prepared in collaboration with SNL personnel. RADLAC results will be presented in a separate, classified report.

Also under the present contract, MRC contributed to a review of Department of Energy in-house nuclear-directed energy programs.

TECHNICAL ISSUES

The production of the IFR channel is fundamental to the guiding of a relativistic electron beam by an ion channel. Photoionization of organic molecules by a UV laser, the most common method of producing these channels, has its drawbacks. The compounds can be difficult to handle. Fragmentation of the molecules complicates the "gas" chemistry. Perhaps most important from the perspective of the basic physics of IFR transport, the range of masses of suitable molecules is limited. To circumvent these difficulties, the possibility of creating an IFT channel using a low energy electron beam is considered in Section II.

In order to fully exploit laboratory scale experiments on IFT transport of intense relativistic electron beams and assess application scale systems, analytic scaling laws for the pertinent physics issues must be developed. Our efforts to do this for certain issues related to beam

equilibrium and stability are described in Section III. Results of numerical simulations to test some of these are presented in Section IV. Section V describes some analytic results related to the dynamics of the ion channel in the absence of a beam. This is a topic of particular importance in recirculating devices.

The transport of beams in curved IFR channels, also essential in recirculating accelerators, presents certain difficulties for numerical solutions by PIC simulation. These systems are fully three-dimensional, and codes for treating three-dimensional problems are enormously expensive to run (if they are available at all). Often, they can only treat the simplest geometry and are not suitable for our purposes. We have developed an approximation scheme to treat IFR transport in curved channels as essentially a quasi-two-dimensional one. This is described in Section VI.

Some energy balance relationships for a beam in an IFR channel are discussed in Appendix A. These have been used to obtain some of the results in Section III and are included for completeness.

II. CHANNEL FORMATION

In this section, we take a preliminary look at the feasibility of using an electron beam to create an IFR channel. The main issue is whether sufficient ionization can be produced over long enough distances and maintained for long enough times. The parameters determining this are the ionization cross sections and pulse length, which affect the magnitude of the ionization; the ionization cross sections, which through the mean free path affect the distance over which the ionization can be formed; and recombination and thermal effects, which impact the lifetime of the channel. For typical parameters, we examine the trade-offs in gas type, pressure, beam energy, current and pulse length for such an ionization channel. This is done for a generic accelerator application and for a proof of concept experiment.

The parameters considered are:

I (current)	< 1 A
L (channel length)	< 100 m
p (pressure)	1 - 5 microns
n_i (ion density)	10^{12} cm^{-3}
E (beam energy)	400 eV - 100 keV

The gases considered are helium, neon, argon and xenon. Molecular species are not considered due to their shorter recombination times.

1. IONIZATION CROSS SECTIONS

In the energy range of 400 eV to 100 keV, ionization cross sections for He, Ne, Ar and Xe vary from 3×10^{-19} cm^2 to 3.5×10^{-16} cm^2. (See Figure 1 and Table 1.[1]) Data for Xe up to 1 keV is from Rapp[2] with an extrapolation performed to higher energies.

TABLE 1. TOTAL CROSS SECTIONS σ_T FOR IONIZATION OF HELIUM, NEON, AND ARGON ATOMS BY ELECTRON IMPACT

Energy (keV)	Cross Sections (cm^2)		
	e + He	e + Ne	e + Ar
2.0 E-02			7.40 E-17
2.5 E-02	8.80 E-19	4.10 E-18	1.50 E-16
4.0 E-02	1.71 E-17	2.30 E-17	2.48 E-16
6.0 E-02	2.99 E-17	4.65 E-17	2.85 E-16
8.0 E-02	3.41 E-17	6.12 E-17	3.00 E-16
1.0 E-01	3.60 E-17	7.00 E-17	3.01 E-16
2.0 E-01	3.38 E-17	8.10 E-17	2.50 E-16
4.0 E-01	2.44 E-17	6.48 E-17	1.80 E-16
8.0 E-01	1.48 E-17	4.27 E-17	1.01 E-16
1.0 E 00	1.22 E-17	3.60 E-17	8.50 E-17
2.0 E 00	6.92 E-18	2.00 E-17	4.70 E-17
3.0 E 00	5.20 E-18	1.41 E-17	3.38 E-17
4.0 E 00	4.19 E-18	1.08 E-17	2.68 E-17
6.0 E 00	3.00 E-18	7.80 E-18	1.98 E-17
8.0 E 00	2.31 E-18	5.90 E-18	1.58 E-17
		Theoretical	
1.0 E 01	1.9 E-18	5.20 E-18	1.20 E-17
1.5 E 01		3.60 E-18	8.20 E-18
2.0 E 01		2.70 E-18	
5.0 E 01	5.1 E 19		
1.0 E 02	3.1 E-19		
5.0 E 02	1.4 E-19		
1.0 E 03	1.3 E-19		
5.0 E 03	1.4 E-19		
1.0 E 04	1.5 E-19		
5.0 E 04	1.8 E-19		
1.0 E 05	1.9 E-19		

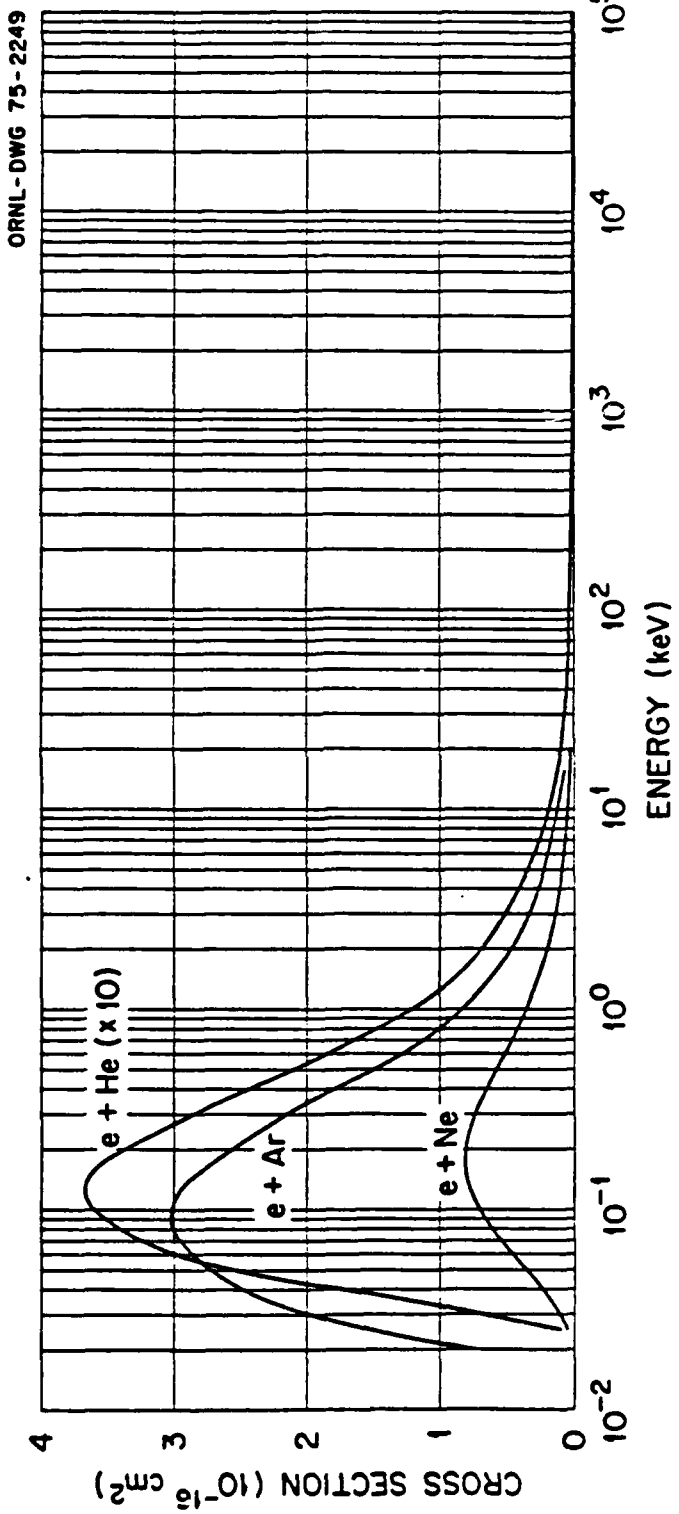

Figure 1. Total cross-section for ionization of helium, argon, and neon by electron impact.

2. MEAN FREE PATH

The mean free path is

$$\lambda(\text{cm}) = 2.82 \times 10^{-15}/p(\text{microns})\sigma(\text{cm}^2)$$

For p = 1 micron and σ in the range mentioned above, λ ranges from 9.4×10^4 cm to 80 cm. These values comfortably span those needed for either an experiment or the application.

3. PULSE LENGTH

Ignoring recombination for the moment, the pulse length needed to give an ion density of n_i is

$$\tau(\text{s}) = n_i\ (\text{cm}^{-3})e(\text{coul})/n_g\ (\text{cm}^{-3})\sigma(\text{cm}^2)j(\text{A/cm}^2)$$

where e is the electron charge and j the current density. If we define the ionization fraction $f_i = n_i/n_g$, then

$$j\tau = f_i\ e/\sigma$$

or in terms of the mean free path,

$$j\tau = n_i \lambda e$$

For p = 1 micron, $n_i = 10^{12}$ cm^{-3}, j = 1 A/cm^2 and σ for He,

E(keV)	τ (ms)
0.4	0.18
1.0	0.37
10.0	2.37

For p = 1 micron, and the rare gases listed earlier, the mean free paths range from 80 cm to 9.4×10^4 cm. The corresponding pulse lengths for j = 1 A/cm^2 range from 12.8 μs to 15.0 ms. Again, the pulse lengths needed are in an achievable range.

4. RECOMBINATION

One recombination mechanism available is radiative recombination. A rough estimate for this recombination time is 0.3 s ($n_i = 10^{12}$, Te = 300°). In practice this would be significantly reduced by impurities, the details of which are hard to estimate. However, collisional-radiative recombination occurs on a shorter timescale and would dominate purely radiative recombination.

The collisional-radiative recombination rate is strongly temperature dependent[3] (see Table 2), so an estimate of the electron temperature must be made. If the temperature is low, the recombination rate may be too rapid for the ion channel to persist. A crude estimate for the electron temperature was made by calculating the equilibrium value of the energy deposited to each gas atom and relating this to the temperature.

$$3/2\ kT = \frac{dE/dx\ \ j\tau}{n_g e}$$

For 1 keV electrons in He,

$$\Delta T = 2.17 \times 10^7 j\tau$$

i.e., for $j = 1\ A/cm^2$ and $\tau = 0.1$ ms, $\Delta T \approx 2200°$. Referring to Table 2 shows that for $n_i = 10^{12}$, the recombination time is increased to an acceptable value around 50 ms.

TABLE 2. COLLISIONAL-RADIATIVE RECOMBINATION TIMES $(n_e\alpha)^{-1}$ IN SECONDS

n_e	T = 500°K	1000°K	2000°K	4000°K	8000°K
10^{10}	6.25(-1)	5.26(0)	2.44(+1)	7.14(+1)	1.64(+2)
10^{11}	1.00(-2)	1.45(-1)	1.10(0)	4.55(0)	1.23(+1)
10^{12}	1.11(-4)	2.56(-3)	3.45(-2)	2.27(-1)	8.33(-1)
10^{13}	1.12(-6)	3.23(-5)	7.14(-4)	8.33(-3)	4.76(-2)

Numbers in parentheses give the power of 10 by which the entries must be multiplied.

5. THERMAL EFFECTS

Another possible mechanism to remove ions is thermal expansion. The time required to do this was estimated by equating the mean kinetic energy to the thermal energy.

$$\bar{v} = \left(\frac{3kT_g}{m}\right)$$

or

$$\bar{v}\ (cm/s) = 1.5 \times 10^4 \left[(T_g\ (°K)/A\ (amu)\right]^{1/2}$$

where A is the atomic mass. The times to travel 1 cm are given in the following table:

		t (μs)			
Atom	$v/T_g^{1/2}$	T_g = 300°	1000°	2000°	4000°
He	7.9×10^3	7.3	4.0	2.8	2.0
Ne	3.52×10^3	16.4	9.0	6.3	4.5
Ar	2.5×10^3	23.1	12.6	8.9	6.3

The above table can also be used to estimate ambipolar diffusion times. The energy gained by a particle traversing the electric field is roughly the temperature of the electrons whose displacement created the field. So, by replacing the gas temperature above, by the electron temperatures, ambipolar diffusion times can be estimated. Thermal expansion and ambipolar diffusion seem to be much more limiting than recombination in determining the lifetime of the channel. However, a magnetic guide field can be used to contain the ions. The gyroradius is:

$$r_i(cm) = 1.02 \times 10^2\ A^{1/2}(amu)\ T_g^{1/2}(eV)\ B^{-1}(gauss)$$

So only a moderate field, B = 170 gauss, is needed to confine a 2000° He ion to r_i = 0.5 cm. A moderate guide field seems to easily overcome the diffusion problems.

6. EXPERIMENTAL PARAMETERS

The following parameters are chosen to check the feasibility of a proof of concept experiment.

$j < 1\ A/cm^2$

L 50 cm

p 1-5 microns of He

n_i $10^{12}\ cm^{-3}$

E 1 keV

For these parameters,

$\sigma = 1.22 \times 10^{-17}\ cm^2$

λ = 462 cm - 23.1 m

$j\tau = 7.4 \times 10^{-5} - 3.7 \times 10^{-4}\ A\ s\ cm^{-2}$

ΔT = 1600-8000° K

τ_{recomb} = 35-830 ms

The 462 cm mean free path corresponds to a 10% loss in 50 cm.

7. APPLICATION PARAMETERS

For an envisioned accelerator application the following parameters are chosen

$j < 1\ A/cm^2$

L 50 m

p 1 micron He

n_i $10^{12}\ cm^{-3}$

E 10 keV

For these parameters,

$\sigma = 1.9 \times 10^{-18}$ cm^2

$\lambda = 150$ m

$j\tau = 2.4 \times 10^{-3}$ A cm^{-2} s

$\Delta T = 8900°$ K

$\tau_{recomb} > 900$ ms

The 150 m mean free path corresponds to a 30% loss in 50 m.

8. CONCLUSION

The most impactive parameter for the concept seems to be temperature. If the electron temperature is too low, recombination will destroy the channel. If the electron temperature is too high, ambipolar diffusion will rapidly expand the channel. However, the application of a moderate guide field is sufficient to overcome the ambipolar diffusion. With such a field, the temperature can be allowed to get high enough that recombination should be no problem. Of course, effects like recombination with electrons streaming off metallic surfaces have been ignored in these first calculations. Additionally, if the conditions are more like a discharge and less like a beam, the analysis changes. The above calculations indicate that sufficient ionization can be created over long enough distances, and it appears that it can be maintained over long enough times.

III. ACCELERATOR IFR BEAM TRANSPORT THEORY

Several important issues must be addressed to assure successful IFR transport in recirculating accelerators: beam and channel equilibrium properties, beam front erosion, beam emittance growth, beam-channel instabilities, and injection and extraction. This section presents analytical estimates for many of these issues and identifies those which require further study.

Two generic recirculating accelerating designs can be envisioned, a racetrack geometry in which the accelerated beam passes around a single closed drift tube many times and a helix geometry in which the beam is injected at one end and extracted at the other. The former entails complex injection and extraction procedures, while the latter is bulkier and, in particular, requires a larger acceleration module bore size.

We assume a relativistic electron beam propagating in an IFR channel of comparable radius approximately centered in a metallic drift tube. The channel to beam line density ratio f is taken to be less than one unless otherwise stated. For f much less than one, the equilibrium channel radius in the presence of the beam is somewhat less than the beam radius, but this should not affect significantly the conclusions of this report. The beam and channel mean radius is designated a, the drift tube radius b, and the drift tube characteristic bending radius R. Approximately gaussian beam and channel radial profiles are assumed. The beam normalized current and energy are ν and γ, respectively.

1. EQUILIBRIUM CONDITIONS

In these terms, the usual radial force balance equation for beam electrons in the partially charged neutralizing ion channel is

$$\frac{\nu}{\gamma}\left[f - \frac{c^2 + p_\perp^2}{\gamma^2 c^2}\right] \approx \frac{p_\perp^2}{\gamma^2 c^2} \tag{1}$$

The average transverse momentum $p_\perp$ can include both thermal and rotational motion. It can be related to an effective normalized emittance, $p_\perp a/c = \varepsilon_n$, which is approximately conserved during acceleration.

$$\frac{\nu}{\gamma}\left[f - \frac{a^2 + \varepsilon_n^2}{\gamma^2 a^2}\right] \approx \frac{\varepsilon_n^2}{\gamma^2 a^2} \tag{2}$$

Provided $f \gg \gamma^{-2}$, the beam always can find an equilibrium radius, although it may exceed the drift tube radius, in which case current loss occurs. For instance, low energy portions of the RADLAC beam, which has high normalized emittance due to rotation, are lost rapidly in IFR transport simulations.[4]

Typically, as low an emittance as possible is desirable in an a celerator. Taking as a lower bound the Lawson-Penner relation,[5] $\varepsilon_n^{LP} \approx \sqrt{\nu}$ rad-cm, gives the simple radial equilibrium expression

$$f\gamma[a(\text{cm})]^2 \approx 1 \tag{3}$$

for $1 > f \gg \gamma^{-2}$. Equation 3 is readily satisfied for even modestly relativistic injection energies. Thus, IFR transport eliminates the need for magnetic focusing in the accelerator. Care should be taken to avoid abrupt changes in the matching condition, which can cause emittance growth and current loss. The beam and channel contract during acceleration in a racetrack geometry. It may be possible in a helix geometry to vary f along the beam path to control the beam radius.

The γ appearing in these equations is, of course, based on beam energy reduced by the space-charge depression, approximately

$$\Delta\gamma = (1 - f)\nu\,(1 + 2\,\ell n\, b/a) \tag{4}$$

for currents below the spacecharge limit,

$$(1 - f)\nu_L = (\gamma_0^{2/3} - 1)^{3/2}/(1 + 2\,\ell n\, b/a) \tag{5}$$

Not surprisingly, these expressions differ from those for vacuum transport only by a factor of f.

If the electron beam in the accelerator is pulsed, the ion column expands electrostatically between pulses with a doubling time of order

$$ct_e \sim \left(\frac{a^2}{\nu f}\frac{m_i}{m_e}\right)^{1/2} \tag{6}$$

For typical parameters $f\nu = 1/2$, $a = 1$, and singly ionized Xenon, the column radius doubles in about 20 ns (see Section V). Less time is required for lighter ions. The channel contracts again with the arrival of the the next pulse. The resulting oscillations of the ion channel increase beam emittance and may trigger instabilities. Keeping the beam interpulse spacing short is highly desirable. Alternatively, it may be possible to neutralize the ion column with electrons injected from the drift tube wall, perhaps by techniques similar to those used in PULSELAC.

2. CHANNEL TRACKING

The electron beam can track a curved ion channel, if its curvature radius is not too small. Balancing electrostatic and centrifugal forces indicates that the beam in a bend displaces by an amount δ from the channel axis,

$$\frac{\delta}{a} \approx \frac{a}{R}\frac{\gamma}{\nu f} \tag{7}$$

The displacement must be somewhat less than the channel radius to prevent significant loss of electrons lying near the edge of the beam emittance

envelope. Recent simulations[6] suggest $\delta/a < 0.2$, limiting the electron energy to 5 MeV or less for $R/a = 100$ and $f_v = 1/2$. This energy limit is less optimistic than our earlier estimate of 15 - 20 MeV for $f_v = 1$, which considered only detracking of the entire beam.[7] The new result is consistent with a recent experiment demonstrating 90% transport of a 1 MeV, 18 kA beam through a 90° turn with $R/a \approx 90$.[8] It is evident, therefore, that the IFR channel cannot replace bending magnets in a recirculating accelerator. The channel does, however, provide about a 10 MeV energy bandwidth, reducing tolerance requirements on the magnetic field.

To the extent that the channel contributes to bending the electron beam, it feels a force and drifts sideways. The time for the channel to move a beam radius is

$$ct_d \sim \left(\frac{2fRa}{\gamma_d}\frac{m_i}{m_e}\right)^{1/2} \tag{8}$$

where γ_d is the beam energy mismatch in the turn. For the parameters used previously, a 2 MeV energy mismatch, and $f = 1/2$, the transverse drift time is 70 ns. Thus, t_d is only about three times the minimum circulation time in a racetrack geometry and may be less than the beam pulselength in a helix geometry.

Channel drift can be reduced by image forces in the drift tube walls, if the drift tube radius is not too large. The net image force is approximately $-2f_v\Delta/b^2$. Hoop stresses are negligible. Balancing the image forces against the centrifugal force and applied magnetic force gives

$$\frac{\Delta}{b} \approx \frac{b}{R}\frac{\gamma_d}{2v_f} \tag{9}$$

or $\Delta = 0.6$ cm for $b = 5$ cm. Channel displacements of this magnitude in turns are acceptable. At transitions between straight and curved drift tube sections, the channel adjusts smoothly over distances of order one-fourth a betatron wavelength. Note that magnetic image forces decay on

tens-of-microsecond timescales, depending on the composition and thickness of the drift tube wall. Acceleration should be completed by that time.

3. BEAM FRONT EROSION

Inductive erosion of a low current beam in a straight drift tube is determined easily. Electrons at the front of the beam lose energy at a rate $f/\nu l \cdot (1 + 2\ \ell n(b/a))$, where l is the length over which the beam magnetic field rises to its full magnitude. Electrons in this length l, which is the greater of the current rise length and the beam radius, continue to drop in energy until they become nonrelativistic, fall behind, and are expelled electrostatically. Hence, after initial transients, which may be quite long for beams injected at high energies, the beam front erosion rate settles to approximately

$$\frac{dx}{dz} \approx \frac{f\nu}{\gamma} (1 + 2\ \ell n\ b/a) \tag{10}$$

where z measures transport distance, and x the length of beam eroded. Most of the lost energy is carried off by expelled channel electrons. The erosion rate varies as $4.2/\gamma$ for the parameters introduced above, severely limiting the minimum practical energy at which the beam can be injected into the accelerator.

A similar calculation shows that the beam tail gains no energy inductively, unless the pulse length is comparable to l. Likewise, the fronts of subsequent pulses lose no energy except to the extent that the channel has captured electrons between pulses.

The validity of this simple analysis becomes questionable as ν approaches unity, because channel electrons attain mildly relativistic energies while being expelled. As a consequence, a portion of the channel electrons are trapped at a few times the beam radius by the beam magnetic field and swept forward with the beam front. This behavior is seen clearly in the simulations described in Section IV, and the corresponding

experiments exhibited current enhancement at the front of the pulse.[8] It is difficult to obtain scalable erosion rates from either the experiments or the simulations, because the injected beam was itself only marginally relativistic and because transport distances were short. Interestingly, recent IFR simulations of higher energy 10 kA beams, performed for other reasons, showed less channel electron trapping than expected.[6] The discrepancy is being investigated. In any event, one might expect the erosion rate to be unchanged to lowest order from trapped channel electrons, since f_v remains the same despite the increase in current locally.

Low energy electrons can be accumulated at the beam head by a second mechanism. Often the acceleration modules are energized slightly before the arrival of the beam, thereby accelerating channel electrons. Travelling more slowly than the main beam, the accelerated channel electrons tend to fall back into the beam head. The significant electron energy spread at the front of the 40 MeV beam emerging from the ATA linear induction accelerator, which uses IFR transport, is attributed to this mechanism.[9] At currents of order 10 kA, magnetic trapping may also have played a role.

Beam bending changes the entire picture. Most channel electrons moving with the beam, including those picked up in straight sections of the accelerator, are lost in the curved sections, unless their energy matches that of the main beam to within the energy bandwidth of the bend. Recall that the bandwidth for loss of the hotter electrons in the beam is at most 10 MeV, and that the comoving channel electrons tend to have high transverse energies.

More seriously, the limited energy bandwidth of the bends may deplete the inductively decelerated beam electrons in the beam front, enhancing inductive erosion. One might imagine as a worst case that γ should be replaced by γ_d in Equation 10, leading to a large erosion rate. More realistically, only a portion of the reduced energy beam particles are lost in the turns, only modestly increasing inductive erosion. The uncertainties here are great.

For completeness, we also mention what might be called centrifugal erosion, although its effect is small. Electrons at the very front of the beam in a turn benefit not at all from the IFR-generated energy bandwidth, because channel electrons are not yet expelled from the channel. The resulting erosion is analogous to that suffered by a beam following a straight IFR channel across a transverse magnetic field.[10] Replacing the magnetic force by the centrifugal force in the semi-analytically obtained magnetic erosion formula[11] yields

$$\frac{dx}{dz} \sim \left(\frac{a}{R}\frac{\gamma_d}{\nu f}\right)^{1.15}\left(\frac{f}{\gamma_d}\right)^{1/2} \tag{11}$$

The centrifugal erosion rate is of order 0.02 for the parameters considered here.

4. BEAM EMITTANCE GROWTH

At each transition between straight and curved sections of the IFR channel in racetrack geometry, the beam equilibrium position abruptly shifts sideways by δ. The beam itself attempts to follow its equilibrium position, overshoots, and oscillates about that position. After a distance of a few wavelengths, the oscillations damp by phase-mixing, leaving the beam with an increased emittance. Since the initial oscillation amplitude is δ, the new emittance may be expected to be

$$\varepsilon_n \sim \varepsilon_n^0\left(1 + \frac{\delta}{a}\right) \tag{12}$$

Rigorous calculations by W. Rienstra give essentially the same result for small δ/a.[12] After twenty cycles with four transitions per cycle, beam normalized emittance grows by three orders of magnitude for $\delta/a = 0.1$. This is clearly unacceptable.

That the beam relaxes in a few betatron wavelengths suggests two methods of reducing emittance growth, by varying the drift tube curvature radius over distances long compared to the betatron wavelength or by having

straight sections of the drift tube short compared to the betatron wavelength. The beam betatron wavelength in the IFR channel is

$$\lambda_\beta = 2\pi a\left(\frac{\gamma}{\nu f}\right)^{1/2} \tag{13}$$

or about $6\gamma^{1/2}$ cm for the parameters used here. Hence, λ_β ranges between 20 cm and 85 cm for energies between 5 MeV and 100 MeV. A roughly ellipsoidal racetrack geometry with straight sections about 20 cm long to accommodate an acceleration module and transition sections about 50 cm long where R decreases to 100 cm from ∞ in the straight section would have either long transition regions or short straight regions compared to the betatron wavelength for the entire 5 - 100 MeV energy range. If longer straight sections are required, to permit many acceleration modules or for other reasons, then 100 cm transition sections probably would be adequate to minimize emittance growth.

Of course, matching the bending magnetic fields precisely to the beam energy, so that $\gamma_d = 0$, also eliminates this source of emittance growth.

In a similar fashion, acceleration modules in curved drift tube sections cause emittance growth, unless the applied transverse magnetic field is appropriately varied across the acceleration gap to balance the increased centrifugal force. Provided the beam never is accelerated out of the energy bandwidth of the turn, the worst case emittance growth due to energy mismatch across an acceleration gap is

$$\varepsilon_n = \varepsilon_n^0\left(1 + \frac{a}{R}\frac{\gamma_m}{\nu f}\right) \tag{14}$$

For a final energy $\gamma_m = 200$, Equation 14 predicts a maximum emittance increase of no more than a factor of five. Even crudely matching the transverse magnetic field to the change in beam energy across the acceleration gap should reduce the emittance growth to a factor of two, which is acceptable.

Emittance increases caused by abrupt lateral displacements of the beam centroid equilibrium position have been considered thus far. Abrupt changes in the beam equilibrium radius have a similar effect. Using Eq. (2) and noting that f is replaced by $f \cdot (a/a_0)^2$ when the beam contracts but the channel does not, we find that the equilibrium radius varies as the fourth root of the beam energy. Arguments resembling those used above then give a cumulative beam emittance growth from gap induced radial oscillations of

$$\varepsilon_n = \varepsilon_n^0 \left(\gamma_m/\gamma_0\right)^{1/4} \tag{15}$$

or a factor of 2.1 for a 5 MeV injection energy. Thin solenoidal lenses placed near the acceleration modules to match the beam initial and final radii might reduce this growth somewhat.

Implicit in the emittance growth estimates presented here is the assumption that the average beam radius does not change greatly during the course of acceleration. Because the beam radius scales as $\varepsilon_n/\gamma^{1/2}$ according to Eq. (2), a twenty-fold increase in beam energy is balanced by 4.5-fold increase in emittance. Such an increase is not unreasonable in light of the previous estimates.

Severe emittance growth is known to occur in low current recirculating accelerators due to particle resonance effects, when the beam betatron frequency is a small integer multiple of the circulation frequency.[13] Similar behavior is unlikely in high current, IFR focused, inductive gap accelerators for several reasons. IFR focusing is nonlinear for large amplitude oscillations, saturating the resonant interaction. The number of betatron wavelengths around the racetrack typically is large, which narrows the resonance bandwidth. The rapid acceleration produced by inductively driven gaps causes the beam to pass through resonances quickly, or miss them entirely.

Emittance growth also is caused by instabilities, the topic of the next subsection.

5. COLLECTIVE INSTABILITIES

The accelerated electron beam may be unstable through interaction with the channel or with the accelerator. The former category consists of hose-like electron and ion two-stream instabilities, while the latter includes principally the negative mass and beam breakup instabilities.

For $f > 1$, only a portion of the channel electrons are expelled by the beam, and the beam is only loosely bound to the channel. Simulations (performed for another project) always exhibit strong instabilities between the beam and remaining channel electrons within a propagation distance of several betatron wavelengths.[14] Both hose and sausage motions are evident, with hose usually dominating. Significant emittance growth and at least some current loss results. Analytic studies have not suggested any method of avoiding this instability except the obvious course of requiring $f < 1$, which we recommend.

The ion two-stream instability, sometimes called the ion resonance instability,[15] occurs for $f < 1$. For $\frac{\gamma m_e}{m_i} \ll 1$, its temporal growth rate at a fixed point in the accelerator is smaller than, the ion plasma frequency based on the beam density,[16]

$$\Gamma < \frac{c}{a} \left(\nu \frac{m_e}{m_i} \right)^{1/2} \tag{16}$$

resulting in an e-folding time of about 20 ns. Consequently, the instability can be avoided in a helix geometry simply by limiting the beam pulse length to 100 ns or so. This option in not available in a racetrack geometry, and acceleration times of 100 ns or less are unrealistic. Therefore, one must rely on effects not yet fully taken into account, such as nonlinearities,[17] multiple ion species, or charge exchange,[18] to reduce instability growth significantly. We remark in this respect that the instability has been observed experimentally for IFR channels in only a few instances.[8] It is conspicuous by its apparent absence in ATA experiment.[19]

The negative mass instability afflicts beams on curved trajectories.[20] Its e-folding time is relatively long, several hundred nanoseconds for parameters of interest. So, it should be of no concern for the rapidly accelerated beam of a recirculating inductive gap accelerator. Focusing provided by the IFR channel also should be stabilizing. The resistive wall instability is slower still, and should be completely negligible.

IFR transport is known both theoretically[21] and from experiments on the ETA and ATA accelerators[22] to suppress cavity-coupled instabilities, such as the beam breakup and image displacement modes in linear induction accelerators. Without ion focusing, beam breakup growth due to low Q gaps typically is slow compared to negative mass growth.[23]

6. INJECTION AND EXTRACTION

Electron beam injection and extraction obviously are no problem in helix geometry. Unfortunately, the same is not true in racetrack geometry.

Substantial thought has gone into this problem for high current betatrons, and the proposed schemes[24,25] may be practical as well for recirculating accelerators with IFR channels. Here, we consider some options unique to IFR transport.

Sloan has shown analytically that an electron beam injected at a small angle to an IFR channel is captured if the injection angle is less than $2(f\upsilon/\gamma)^{1/2}$.[26] This angle is 36° for a 5 MeV injection energy. However, by analogy with channel tracking around a curve, we expect that a much smaller angle should be used to avoid loss of beam current. Only a 50 cm straight drift tube section would be needed to capture the beam injected at 6° with $b = 5$ cm. Conceivably, the magnetic fringing field at the transition to a curved section could be employed to shorten this distance modestly. Emittance growth in the injection process can be as low as the ratio of the injection angle to the maximum injection angle, or just under 20%.

An IFR-based extraction scheme is less obvious. A weak, localized, transverse magnetic field not quite sufficient to deflect the beam from the channel could be applied in a straight section of the accelerator. Then, a laser beam fired into the transverse field region at a glancing angle to the original channel would create a new channel which the beam might follow out of the accelerator. The loss of beam quality which might result is unknown.

B. Hui and Y. Lau have proposed analogous schemes for injection and extraction in a modified betatron.[27]

7. SUMMARY AND RECOMMENDATIONS

The preceding discussions suggest that inductive erosion in curved channels, emittance growth at transitions between straight and curved drift tube sections, ion two-stream instabilities, and beam extraction (in race-track geometry) are the most serious uncertainties confronting IFR transport for recirculating accelerators. Our understanding of streaming instabilities under realistic conditions can be improved with more detailed linear analyses. Single particle calculations can provide a useful basis for emittance growth assessments. Extraction simply needs new ideas. Beyond this, multi-dimensional computer simulations and parallel experiments are required. Beam extraction and ion instability growth and saturation can profitably be addressed with the simulation techniques employed in obtaining the preliminary transport results presented in the next section. The nearly completed code modifications outlined in Section V are necessary to treat erosion and emittance growth in curved channels properly.

IV. MIMI SIMULATIONS

In this section we give a brief description of several computer simulations which were done to address the issue of the inductive erosion of low ν/γ beams in IFR channels. The parameters used in the simulations were typical of those in experiments performed at the MIMI facility at Sandia National Laboratory.

A relativistic electron beam of energy, $\gamma = 4.0$ and current, $I_b = 10$ kA was injected into an IFR channel of line density ratio, $f = 1$. The beam and channel were assumed to be of equal radii, $a = 7$ mm. The channel was centered in a conducting drift pipe. Two different pipe radii were used in the simulations, 20 cm and 5 cm.

The simulation of the transport in a 20 cm drift pipe showed an erosion rate of approximately 60%-70%. The erosion rate in the smaller pipe was reduced from that in the larger pipe by about 25% to a rate of approximately 35%-45%. Because the beam energy is so low, the inductive γ depression is large enough to diminish the velocity of the beam head substantially making it difficult to precisely define the pinch point. This is the reason for the uncertainty in the erosion rate values. Particle plots for the two cases are shown in Figure 2.

The erosion rates observed in the simulations are smaller by about a factor of two from those calculated from Equation 10, Section III. This discrepancy is likely due to the trapping of the channel electrons by the self magnetic field of the beam. It is observed in the simulation that the channel electrons are driven forward (along the beam) due to the $E \times B$ drift in the radial electric field and azimuthal magnetic field of the beam. This is consistent with estimates of the gyroradius of a channel electron in the field of the beam. The estimates show the gyroradius to be smaller than or of the order of the channel radius. The snapshots of Figure 2 do not illustrate this effect well, but it is very clear in

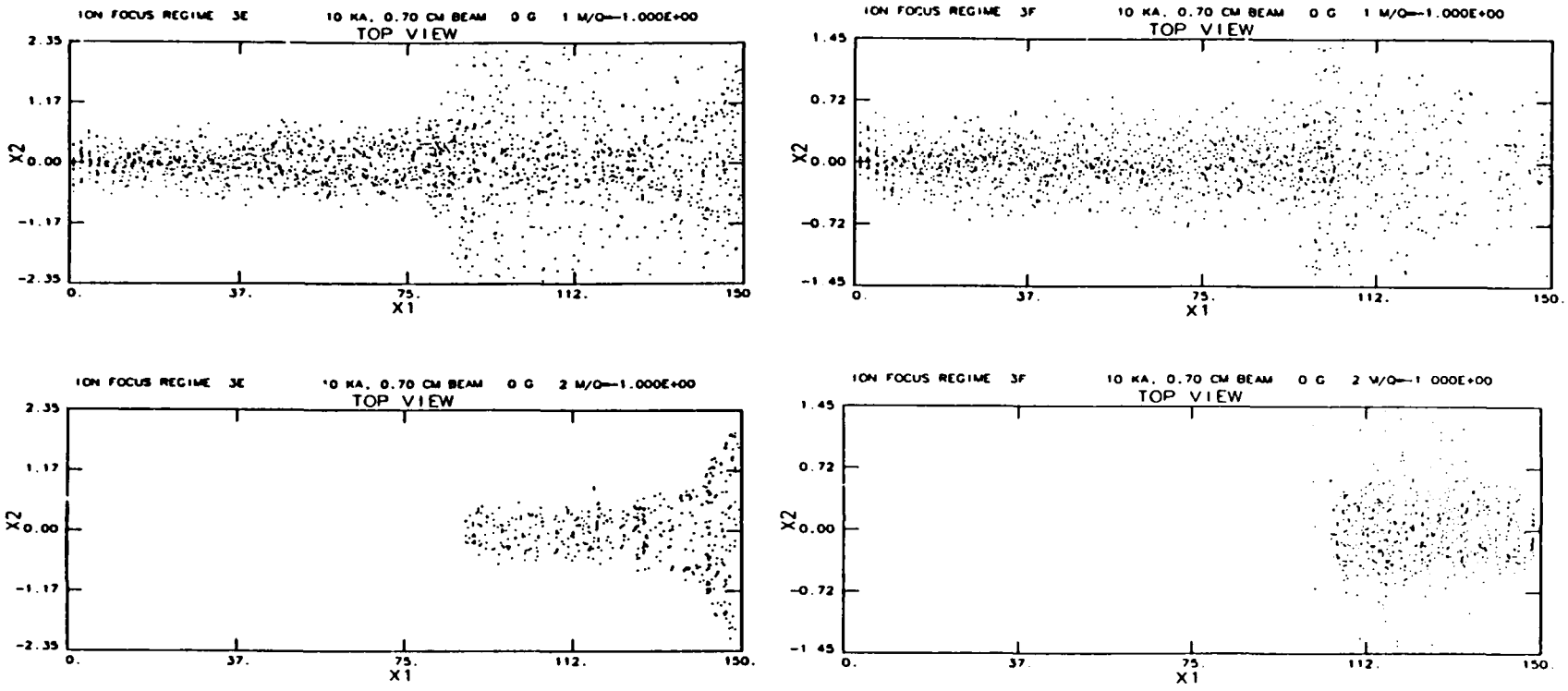

(a) (b)

Figure 2. Beam and plasma electron particle plots, 4 MeV, 10 kA beam in an f = 1 IFR channel. Drift tube radii are (a) 20 cm and (b)5 cm.

motion pictures of the simulation. Furthermore, the net current plots show a considerable current enhancement due to the co-moving channel electrons. This clearly illustrated in Figure 3. The current enhancement is consistent with the experimental observation.[10]

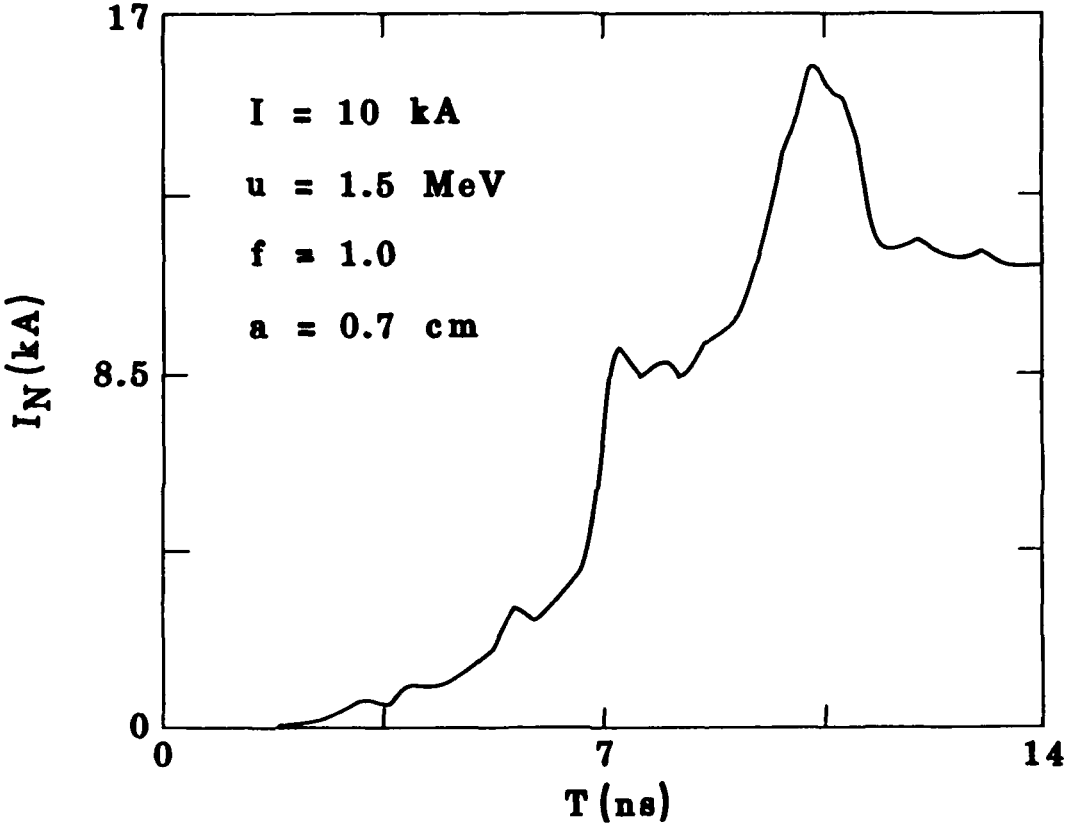

NET CURRENT PROFILE AFTER 1.5 m TRANSPORT

Figure 3. Net current versus time, 10 kA, 4 MeV beam in f = 1 IFR channel. Peak current exceeds beam current (see text).

V SELF EXPANSION OF AN ION CHENNEL

In the IFR transport of an electron beam, the plasma electrons created during the ionization of the channel will be expelled by the stiffer electron beam. If the channel is to be used to guide several beam pulses, the bare ion channel cannot be allowed too much expansion in its self field or it will no adequately beind the beam. An estimate of the expansion of a bare ion channel can be easily made.

If the channel is taken to be axisymmetric and finite in radius, the peak radial self electric field occurs at the channel edge. If, in addition, the channel ions are assumed to be cold, no ion can cross the channel edge. A simple edge envelope equation can then be simply derived using only charge conservation and Gauss' law.

If $a = a(t)$ denotes the instantaneous position of the channel edge, the radial electric field at the edge is

$$E_r = \frac{2Q'}{a(t)} \quad , \quad Q' = 2\pi q \int_0^{a_0} n(r) r dr \tag{17}$$

where a_0 is the initial radius of the channel, q the ion charge, and $n(r)$ the initial channel density profile. Q' is simply the charge per unit length of channel. Under the assumptions made, the motion of the channel edge is independent of the density profile. The equation of motion is

$$M_i \ddot{a} = qE_r = \frac{2qQ}{a(t)} \tag{18}$$

This equation is nonlinear but can be reduced to quadrature. Normalizing the envelope radius to its initial value, a_0, and time to the "time constant" $a_0/\sqrt{2K}$, $K = 2qQ'/M$, the solution can be found in terms of the well known plasma dispersion function, Z:[30]

$$\tau = -\tilde{a}\ \mathrm{Re}[Z(\sqrt{\ell n \tilde{a}})] \tag{19}$$

where

$$\tau = a_0 t/\sqrt{2K}$$

and

$$\tilde{a} = a/a_0$$

This equation gives the time it takes the channel to expand by a factor $\tilde{a}$ over its initial radius. Physically this result is reasonable. For $\tilde{a}$ very large, such that $\ell n\tilde{a} \gg 1$, the asymptotic behavior of τ is

$$\tau \sim 2\tilde{a}/(\ell n\tilde{a})^{1/2} \tag{20}$$

The expansion rate is slower than that for expansion under the action of a uniform field, $\tau \sim \sqrt{\tilde{a}}$ but faster than free expansion, $\tau \sim \tilde{a}$, although just barely in the latter case. For typical cases of interest, the numerical value of ReZ is near unity.

Numerically these times are short for parameters of interest. For example, for an initial radius of 1 cm, $n_i = 10^{12}$ of X_e^+, the doubling time of the channel radius is 19 ns. The scaling is, for singly ionized molecules,

$$t_D(\tilde{a} = 2) = 1.53\, a_0 A^{1/2}\left(\frac{I_A}{fI_b}\right)^{1/2} \quad \text{ns} \tag{21}$$

where A is the atomic number, $I_A = 17$ kA, I_b, the beam current, and f the channel to beam line density ratio. The time for the channel radius to increase an order of magnitude is

$$t_{10} = 6.05\, a_0 A^{1/2}\left(\frac{I_A}{fI_b}\right)^{1/2} \quad \text{ns} \tag{22}$$

The corresponding velocities can also be obtained. The velocity scales as

$$a = (2K)^{1/2} \, (\ell n \tilde{a})^{1/2} \tag{23a}$$

or

$$a = \frac{1.4 \times 10^9}{A^{1/2}} \left(\frac{f I_b}{I_A} \right)^{1/2} \quad \text{cm/s} \tag{23b}$$

At the doubling radius, for $n_i = 10^{12}$ ($I_b = 15$ kA), X_e^+, the velocity is

$$a(\tilde{a} = 2) = 9.6 \times 10^7 \quad \text{cm/s}$$

It is clear the channel expansion can be quite rapid even for massive ions. This could be prevented by refilling the channel with electrons. These could, in the context of a recirculating accelerator, be waste beam. They might also be supplied from the drift pipe wall. In this case the beam would have to clear the channel with each pass and the consequent erosion may be prohibitive. Should this be an option, we have considered the possibility of using a felt cloth liner on the drift pipe as an electron source. Adler and co-workers have shown this material to be an effective source of electrons when used as a field emission cathode.[29] In this application, the turn on time of the cloth fiber is comparable to the risetime of the voltage pulse. In order to be effective, the cloth must emit a sufficient number of electrons before the channel moves appreciably. Current densities of the order of 270 A/cm^2 have been observed in Reference 29. The ion column considered earlier has a line charge $Q' \simeq 1.5 \times 10^3$ esu/cm. A liner on a 4 cm radius drift pipe could be expected to emit 3400 A/cm of drift pipe. The liner therefore must emit for

$$t_e = \frac{1.5 \times 10^3 \text{ esu/cm}}{3400 \text{ A/cm}} \simeq 150 \text{ ps}$$

This is short enough to provide channel neutralization with negligible ion motion.

VI. BEAM TRANSPORT IN CURVED SECTIONS: A COMPUTATIONAL APPROACH

1. THEORY

Theoretical investigation of beam behavior in recirculating accelerators imposes the obvious requirement that some method be adopted for treating the physics in a curved geometry. This is true if analytic solutions to a particular question are sought or if the problem at hand is to be attacked by computer simulation. In this section, a method for solving this problem will be described. It has been used to investigate some linear stability issues in betatrons and has also been implemented in the MRC PIC simulation code IVORY. The latter application will be described in the following part. Before proceeding to discuss the formalism, it is useful to briefly indicate the technical issue which underlies the problem.

Simply stated, the problem is that of finding an appropriate choice of coordinate system in which to describe the physics of the problem. The physics is little more than Newton's equations of motion and Maxwell's equations along with the appropriate boundary conditions. The choice is complicated by the difficulty that in typical systems of interest the simplest coordinate system for the description of the dynamic equations is not the best system for the applications of boundary conditions. Thus, for example, the standard cylindrical system (R, ϕ, Z) of Figure 4 (a) is not well suited to treat transport in curved tubes of circular cross section. The boundary conditions are difficult to describe analytically, leading to infinite series which are slow to converge and thus cumbersome to implement numerically. In the context of a PIC simulation, the best one can hope to do is a piecewise linear fit to the R-Z boundary surface. This can be complicated to implement if the fit must be done accurately. This could be expected to be important in problems where image forces play a role in the physics. Despite these shortcomings, the resulting field equations have well known properties. Furthermore, the symmetry direction, ϕ in Figure 4, can be treated computationally as well as analytically, by Fourier

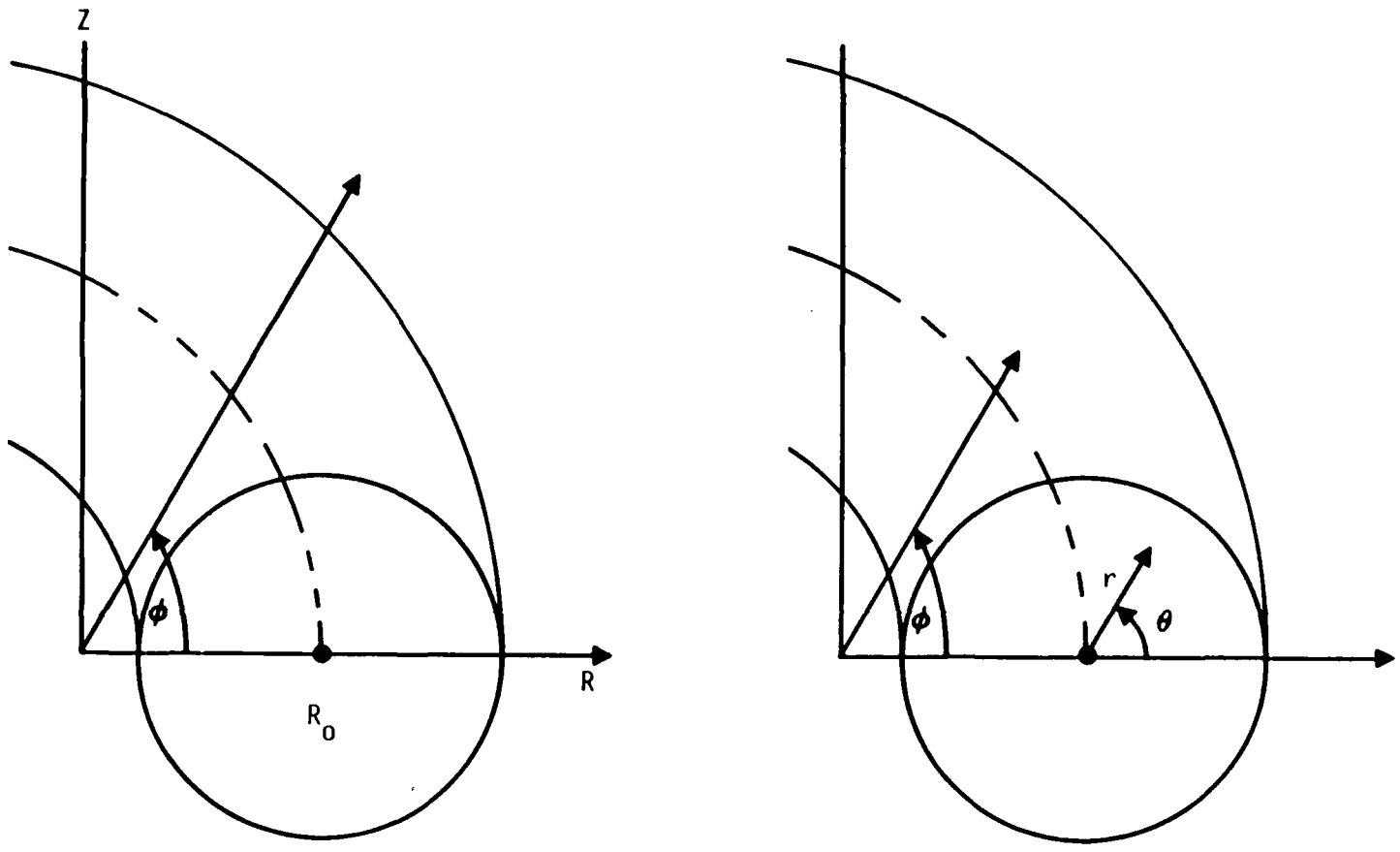

(a) Cylindrical polar

(b) Quasi-toroidal

Figure 4. Coordinate systems for describing beam transport in curved drift pipes.

decomposition and the Fourier mode numbers are good "quantum" numbers. This simplifies three-dimensional simulations, but precludes, a priori the treatment of more complicated geometries such as a racetrack, a configuration of some interest.

An alternative coordinate system might be the (r, θ, ϕ) in Figure 4(b) which we call quasi-toroidal coordinates. In this system, the boundary conditions in a curved tube of circular cross section, the example above, are particularly simple since the boundary surface coincides with a coordinate surface. (Other boundary surfaces, for example elliptic cross sections, could be treated similarly.) The simplicity of the boundary conditions is accompanied, however, by a complication in the equations describing the physics and desirable properties[30] of some of the operators are lost. Furthermore, Fourier decomposition in the angular coordinate, θ, is no longer straightforward in that the modes are no longer good "quantum" numbers. The toroidal curvature couples modes. Fourier decomposition in the ϕ direction remains the same although it is no longer essential or particularly advantageous. We will return to this point. Given these added complications, it is not immediately obvious there is any advantage in employing quasi-toroidal coordinates over cylindrical coordinates, for example. The element that resolves this dilemma is the relative size of the radius of the cross section (minor radius) of the system to the turning radius (major radius). This ratio, the inverse aspect ratio, is typically small and provides an expansion parameter in the quasi-toroidal coordinate system. In this way, the properties of a simple coordinate system can be recovered. Furthermore, the mode coupling in a Fourier decomposition in the poloidal angle, θ, can be related to the order of the expansion in the inverse aspect ratio. This allows the mode coupling to be calculated explicitly. In implementing this procedure in PIC simulation codes, the toroidal angle, ϕ, can be treated as a mesh coordinate, along with ρ. By doing this, racetrack-like geometries can be treated in contrast to the case employing a cylindrical coordinate system. This is the point of employing Fourier transformed representation in the poloidal angle with the mode coupling given explicitly. Thus, in the small

inverse aspect ratio approximation, the use of a quasi-toroidal coordinate system manifests clear advantages. We will now describe the formalism generated by this approach.

The basic entities which are required to describe the dynamical equations in any coordinate system are the various vector differential operators which operate on the field quantities which appear in the equations of motion, Maxwell's equations being the equations of motion of the electromagnetic field. The quasi-toroidal coordinate system is orthogonal, and the calculation of these operators proceeds in the standard way.[31] The expressions for the operators will not be given here but, the basic quantities needed to generate them, the metric coefficients, are

$$h_\rho = a \tag{24a}$$

$$h_\theta = a\rho \tag{24b}$$

$$h_\xi = a(1 + a\rho/R_0 \cos\theta) \tag{24c}$$

where normalized coordinates have been introduced by the definitions

$$\rho = r/a \quad , \quad \xi = R_0\phi/a$$

and a measures the minor radius of the system and R_0 is the major radius of curvature as shown in Figure 4. This normalized coordinate system is particularly convenient in that it displays the small parameter, the inverse aspect ratio $\epsilon = a/R_0$, explicitly. The difficulty discussed earlier in implementing this coordinate system in general manifests itself in the dependence of the metric coefficient h_ξ, Eq. 24c, on the poloidal angle θ. This implies a lack of separability[30] and not only complicates general analytic approaches, but also precludes direct numerical simulation. Thus, to proceed, the small inverse aspect ratio expansion is adopted. If $\vec{A}$ represents an arbitrary vector (it could be $\vec{E}$ or $\vec{B}$, for example), we put

$$\vec{A} = \vec{A}^{(0)} + \varepsilon\vec{A}^{(1)} + \ldots \tag{25}$$

The vector operators, because they depend on the metric coefficients, also have an inverse aspect ratio expansion, for example the curl is, symbolically,

$$\nabla X \equiv (\nabla X)^{(0)} + \varepsilon(\nabla X)^{(1)} + \ldots \tag{26a}$$

and similarly the divergence

$$\nabla\cdot \equiv (\nabla\cdot)^{(0)} + \varepsilon(\nabla\cdot)^{(1)} + \ldots \tag{26b}$$

In these expressions and all to follow, the superscript in parentheses will denote the order of the expansion. The expansion generates a set of dynamical equations for the field quantities $\vec{A}^{(m)}$, order by order in ε. The resulting equations can either be solved analytically by, for example, making a linearization and examining stability or implemented in a finite-difference scheme in a simulation code. The formalism is systematic in that, in principle, a calculation can be carried to arbitrary order in ε. In practice, going beyond second order is not likely to be feasible. Before writing the field equations, one final technical point will be mentioned.

In any curvilinear coordinate system, the divergence of the curl of an arbitrary vector field vanishes identically. As described above, our expansion procedure means that the exact operators are replaced by approximate operators. The question arises whether this condition persists when the operators and the arbitrary vector are expanded in ε. This has important physical consequences. Should this fail, charge conservation would no longer hold in each order and this would effectively lead to fictitious charges appearing in numerical simulations. We have resolved this issue by proving $(\nabla \cdot \nabla x\vec{A})^{(n)}$, the nth approximation to $\nabla \cdot \nabla x\vec{A}$ vanishes identically for each n. The proof is by induction but will not be given here. The conclusion is the inverse aspect ratio expansion does not destroy charge conservation independent of the order at which the approximation is truncated. We now proceed to write down the Maxwell equations to first order in ε and discuss their implementation.

The representation of the electromagnetic fields is as in the cylindrical case, a superposition of Fourier modes in the poloidal angle θ. As discussed earlier, the toroidicity now couples modes. The coupling, to first order in ε, is fairly simple. It introduces sidebands $m \pm 1$ on a fundamental mode of frequency m. The amplitude of the sidebands are $O(\varepsilon)$ relative to the fundamental. The mode coupling becomes more complicated in higher order but can be calculated if necessary. For most problems of physical interest only the first order terms are required. For example, if the inverse aspect ratio, $\varepsilon = 30\%$, a fairly large value, the second order terms make only a contribution of approximately 5%. We have only considered the first order terms in the code development effort. In this case, the Maxwell equations for the mth Fourier mode and its sidebands become, introducing the notation

$$Q_{\nu}^{(0)} = Q_{\nu c}^{(0)} \cos m\theta + Q_{\nu s}^{(0)} \sin m\theta$$

$$Q_{\nu\pm}^{(1)} = Q_{\nu c\pm} \cos (m \pm 1)\theta + Q_{\nu s\pm}^{(1)} \sin (m \pm 1)\theta$$

for the νth component of the quantity Q in the $n = 0, 1$ order of approximation:

Faraday's Law

$n = 0$,

$$a\rho \frac{\partial B_{\rho c}^{(0)}}{\partial t} = mE_{\xi s}^{(0)} - \frac{\partial E_{\theta c}^{(0)}}{\partial \xi} \tag{27a}$$

$$a\rho \frac{\partial B_{\rho s}^{(0)}}{\partial t} = -mE_{\xi c}^{(0)} - \frac{\partial E_{\theta s}^{(0)}}{\partial \xi} \tag{27b}$$

$$a \frac{\partial B_{\theta c}^{(0)}}{\partial t} = \frac{\partial E_{\rho c}^{(0)}}{\partial \xi} - \frac{\partial E_{\xi c}^{(0)}}{\partial \rho} \tag{27c}$$

$$a\frac{\partial B^{(0)}_{\theta s}}{\partial t} = \frac{\partial E^{(0)}_{\rho s}}{\partial \xi} - \frac{\partial E^{(0)}_{\xi s}}{\partial \rho} \tag{27d}$$

$$a\rho\frac{\partial B^{(0)}_{\xi c}}{\partial t} = \frac{\partial}{\partial \rho}\left(\rho E^{(0)}_{\theta c}\right) - mE^{(0)}_{\rho s} \tag{27e}$$

$$a\rho\frac{\partial E^{(0)}_{\xi c}}{\partial t} = \frac{\partial}{\partial \rho}\left(\rho E^{(0)}_{\theta s}\right) + mE^{(0)}_{\rho c} \tag{27f}$$

$n = 1,$

$$-\frac{a\rho}{c}\frac{\partial B^{(1)}_{\rho c\mp}}{\partial t} = (m \mp 1)\, E^{(1)}_{\xi s\mp} - \frac{\rho E^{(1)}_{\theta c\mp}}{\partial \xi} + \frac{\rho^2}{2}\frac{\partial E^{(0)}_{\theta c}}{\partial \xi} \mp \frac{\rho E^{(0)}_{\xi s}}{2} \tag{28a}$$

$$-\frac{a\rho}{c}\frac{\partial B^{(1)}_{\rho s\mp}}{\partial t} = (m \mp 1)\, E^{(1)}_{\xi c\mp} - \frac{\rho E^{(1)}_{\theta s\mp}}{\partial \xi} + \frac{\rho^2}{2}\frac{\partial E^{(1)}_{\theta s}}{\partial \xi} \mp \frac{\rho E^{(0)}_{\xi c}}{2} \tag{28b}$$

$$-\frac{a}{c}\frac{\partial B^{(1)}_{\theta c\mp}}{\partial t} = \frac{\partial E^{(1)}_{\rho c\mp}}{\partial \xi} - \frac{\partial E^{(1)}_{\xi c\mp}}{\partial \rho} - \frac{E^{(0)}_{\xi c}}{2} - \frac{\rho}{2}\frac{E^{(0)}_{\rho c}}{\partial \xi} \tag{28c}$$

$$-\frac{a}{c}\frac{\partial B^{(1)}_{\theta s\mp}}{\partial t} = \frac{\partial E^{(1)}_{\rho s\mp}}{\partial \xi} - \frac{\partial E^{(1)}_{\xi s\mp}}{\partial \rho} - \frac{E^{(0)}_{\xi_s}}{2} - \frac{\rho}{2}\frac{E^{(0)}_{\rho_s}}{\partial \xi} \tag{28d}$$

$$-\frac{a\rho}{c}\frac{\partial B^{(1)}_{\xi c\mp}}{\partial t} = \frac{\partial}{\partial \rho}\left(\rho E^{(1)}_{\theta c\mp}\right) \mp (m \mp 1)\, E_{\rho s\mp} \tag{28e}$$

$$-\frac{a\rho}{c}\frac{\partial B^{(1)}_{\xi s\mp}}{\partial t} = \frac{\partial}{\partial \rho}\left(\rho E^{(1)}_{\theta s\mp}\right) \pm (m \mp 1)\, E^{(1)}_{\rho c\mp} \tag{28f}$$

Ampere's Law

$n = 0$,

$$\frac{a\rho}{c}\frac{\partial E^{(0)}_{\rho c}}{\partial t} = \frac{-4\pi a\rho}{c} J^{(0)}_{\rho c} + mB^{(0)}_{\xi s} \tag{29a}$$

$$\frac{a\rho}{c}\frac{\partial E^{(0)}_{\rho s}}{\partial t} = \frac{-4\pi a\rho}{c} J^{(0)}_{\rho s} + mB^{(0)}_{\xi c} \tag{29b}$$

$$\frac{a}{c}\frac{\partial E^{(0)}_{\theta c}}{\partial t} = -4\pi J^{(0)}_{\theta c} + \frac{\partial B^{(0)}_{\rho c}}{\partial \xi} - \frac{\partial B^{(0)}_{\xi c}}{\partial \rho} \tag{29c}$$

$$\frac{a}{c}\frac{\partial E^{(0)}_{\theta s}}{\partial t} = -4\pi J^{(0)}_{\theta s} + \frac{\partial B^{(0)}_{\rho s}}{\partial \xi} - \frac{\partial B^{(0)}_{\xi s}}{\partial \rho} \tag{29d}$$

$$\frac{\rho a}{c}\frac{\partial E^{(0)}_{\xi c}}{\partial t} = -4\pi J^{(0)}_{\xi c} + \frac{\partial}{\partial \rho}\left(\rho\, B^{(0)}_{\theta c}\right) - mB^{(0)}_{\rho s} \tag{29e}$$

$$\frac{\rho a}{c}\frac{\partial E^{(0)}_{\xi s}}{\partial t} = -4\pi J^{(0)}_{\xi s} + \frac{\partial}{\partial \rho}\left(\rho\, B^{(0)}_{\theta c}\right) - mB^{(0)}_{\rho c} \tag{29f}$$

and $n = 1$,

$$\frac{a\rho}{c}\frac{\partial E^{(1)}_{\rho c\mp}}{\partial t} = \frac{-4\pi\rho a}{c} J^{(1)}_{\rho c\mp} + (m \mp 1)\, B_{\xi s\mp} - \frac{\rho \partial B^{(1)}_{\theta c\mp}}{\partial \xi} \pm \frac{\rho}{2} B^{(0)}_{\xi s}$$

$$+ \frac{\rho^2}{2}\frac{\partial B^{(0)}_{\theta c}}{\partial \xi} \tag{30a}$$

$$\frac{a\rho}{c}\frac{\partial E^{(1)}_{\rho s\mp}}{\partial t} = \frac{-4\pi\rho a}{c} J_{\rho s\mp} - (m \mp 1) - \frac{\rho \partial B^{(1)}_{\theta s\mp}}{\partial \xi} - \frac{\rho}{2} B^{(0)}_{\xi c}$$

$$+ \frac{\rho^2}{2}\frac{\partial B^{(0)}_{\theta s}}{\partial \xi} \qquad (30b)$$

$$\frac{a}{c}\frac{\partial E^{(1)}_{\theta c\mp}}{\partial t} = -4\pi J^{(1)}_{\theta c\mp} + \frac{\partial B^{(1)}_{\rho c\mp}}{\partial \xi} - \frac{\partial B^{(1)}_{\xi c\mp}}{\partial \rho} - \frac{B^{(0)}_{\xi c}}{2} - \frac{\rho}{2}\frac{\partial B^{(0)}_{\rho c}}{\partial \xi} \qquad (30c)$$

$$\frac{a}{c}\frac{\partial}{\partial t} E^{(1)}_{\theta s\mp} = -4\pi J^{(1)}_{\theta s\mp} + \frac{\partial B^{(1)}_{\rho s\mp}}{\partial \xi} - \frac{\partial B^{(1)}_{\xi s\mp}}{\partial \rho} - \frac{B^{(0)}_{\xi s}}{2} - \frac{\rho}{2}\frac{\partial B^{(0)}_{\rho s}}{\partial \xi} \qquad (30d)$$

$$\frac{\rho c}{a}\frac{\partial}{\partial t} E^{(1)}_{\xi c\mp} = -4\pi J^{(1)}_{\xi c\mp} + \frac{\partial}{\partial \rho}\ \rho B^{(1)}_{\theta c\mp} - (m \mp 1)\ B^{(1)}_{\rho s\mp} \qquad (30e)$$

$$\frac{\rho c}{a}\frac{\partial E^{(1)}_{\xi s\mp}}{\partial t} = -4\pi J^{(1)}_{\xi s\mp} + \frac{\partial}{\partial \rho}\ \rho B^{(1)}_{\theta s\mp} + (m \mp 1)\ B^{(1)}_{\rho c\mp} \qquad (30f)$$

2. COMPUTATIONAL SCHEME

The equations described in the previous subsection are solved as an initial value problem. The condition $\nabla \cdot \vec{B} = 0$ is an initial condition. Provided div (curl) $\equiv$ 0, as discussed earlier, it is satisfied for all time. Gauss' law is satisfied by insuring charge conservation. It is not solved explicitly. This is the approach used in all of the MRC PIC simulation codes to date.[32]

3. CODE DEVELOPMENT

Application of this method was carried out by modifying the existing 3-D particle-in-cell code IVORY (originally developed by MRC for LANL). IVORY is an electromagnetic relativistic code that solves an initial value problem by pushing particles in the 3-D spatial and velocity phase-space, then projecting particle currents on a 2-D spatial grid with the third dimension resolved into Fourier normal modes. These currents are used subsequently as inputs to the time-dependent Maxwell's equations, advancing self-consistent field quantities for use in the next particle push. Each Fourier component (sine or cosine) is advanced independently (over the same time step). Because IVORY already has the capability to treat Fourier components in one of the three spatial dimensions, it is straightforward, in principle, to modify the field solver to generate the side-band contributions (using the analytic, first-order curl approximations just describeddescribed) in the curved region and calculate the corresponding forces on the particles.

An additional complication arises from the dependence of the metric on the poloidal angle, θ. The current density "J" is calculated from the particle current by dividing by an appropriate metric quantity which includes a first-order "$\varepsilon\cos\theta$" term (from Eq. 24c). This introduces contributions from J of order m to J of order m + 1 cosine mode (assuming $\varepsilon \ll 1$). For the present case, a term of order $J^{(0)}\varepsilon$ must be subtracted from the $J^{(1)}$ cosine term locally on the grid. Because a similar metric division occurs in calculating the charge density "ρ", the continuity equation $\partial\rho/\partial t + \nabla \cdot J = 0$ is still conserved to limits set only by the differencing scheme used.

IVORY has been modified to include the first-order sideband contribution arising from toroidal curvature for the m = 0 poloidal mode in the field solver and to push particles in a toroidal coordinate system. Extensive testing of toroidal particle transport has been performed using several test cases at low current to verify the particle-pushing algorithm and to check

the accuracy of the externally imposed betatron magnetic fields and has yielded satisfactory results. The field solving section is now undergoing testing at high currents.

This is adequate to treat most problems of physical interest. The equilibrium offset of a beam from the minor axis due to the toroidicity corresponds to an $O(\varepsilon)$ excitation of the m = 1 mode in the equilibrium. This is accounted for automatically in the solution of the initial value problem. If the beam is injected with a large offset, corresponding to a large amplitude m = 1 fundamental with sidebands at m = 0 and m = 2, our numerical implementation is inadequate. This is due to the aliasing of the toroidicity sidebands with the nonlinear mode coupling excitations at m = 0 and m = 2. This case could be handled by treating the first order in ε particle push explicitly. The cost is additional complexity of manipulating field quantities. Programming tricks to keep the storage requirements within limits would very likely be necessary.

It also is possible to add an "ionization package" to allow the initialization and subsequent maintenance of a heavy ion channel to guide the beam and partially neutr lize its space charge (which unneutralized is responsible for significant emittance growth). Such a package has already been developed for IVORY to study beam transport in the LEBT region of White Horse for LANL AT division. Parametric studies should yield useful information in support of betatron injection experiments, indicating parameter regimes that minimize emittance growth and beam drift during this critical phase.

4. SUMMARY

A method for performing PIC simulations of charged particle beams in recirculating geometries has been described. Because these simulations are fully three-dimensional, there is no ignorable coordinate and methods which rely on Fourier decomposition must be modified to handle these problems. An approximation scheme for doing this forms the basis of our approach.

The expansion parameter introduced is sufficiently small in typical systems of interest to permit truncation of the approximations in low order and this makes the method practical.

REFERENCES

1. C. F. Barnett, et al, "Atomic Data For Controlled Fusion Research", Oakridge National Laboratory, ORNL-5206, February 1977.

2. D. Rapp, P. Englander-Golden, J. Chem. Phys. 40, 3263 (1964).

3. D. R. Bates and A. Dalgarno, "Electronic Recombination", in Atomic and Molecular Processes, D. R. Bates, Ed., Academic Press, New York, N.Y., 1962.

4. B. B. Godfrey, in preparation.

5. J. Lawson, The Physics of Charged-Particle Beams, (Clarendon Press, Oxford, 1977).

6. M. Mostrom and B. Newberger, unpublished.

7. B. Godfrey, B. Newberger, L. Wright, C. Frost, and S. Shope, in Proc. 1985 SDIO/DARPA/Services Propagation Review, to be published (Secret); also, in "Presentations to SDIO/DARPA/Service Propagation Review Meeting," AMRC-R-721 (Mission Research Corporation, Albuquerque, 1985).

8. S. L. Shope, C. A. Frost, G. T. Leifeste, C. E. Crist, P. D. Krekel, J. W. Poukey, and B. B. Godfrey, IEEE Nuc. Sci., to be published.

9. F. Chambers, et. al., in Proc. 1985 SDIO/DARPA/Services Propagation Review, to be published (Secret).

10. H. L. Buchanan, "Magnetic Erosion Calculations for the 'Antigone' Hybrid Hybrid Transport Scheme," UCID-19501 (Lawrence Livermore National Laboratory, Livermore, 1981).

11. B. B. Godfrey, D. Mitrovich, and L. A. Wright, "Magnetic Erosion Calculations," AMRC-R-551 (Mission Research Corporation, Albuquerque, 1984) (Secret).

12. W. Rienstra, "Curved Channel Emittance Growth," unpublished (1985).

13. D. Chernin and P. Sprangle, Part. Accel. 12, 101 (1982), and references therein.

14. B. Newberger, B. Godfrey, L. Feinstein, and C. Yee, in Proc. 1985 SDIO/DARPA/Services Propagation Review, to be published (Secret).

15. W. M. Manheimer, Part. Accel. 13, 209 (1983).

16. H. S. Uhm and M. Lampe, in Proc. 1984 DARPA/Services Propagation Review, CONF-8406133 (Lawrence Livermore National Laboratory, Livermore, 1984), p. 445 (Secret).

17. H. L. Buchanan, "Linear and Nonlinear Calculations of the Hose Instability in the Ion Focus Regime," UCID-19495 (Lawrence Livermore National Laboratory, Livermore, 1982).

18. S. Yu and G. Caporaso, private communication (1985).

19. D. S. Prono, et al, IEEE Trans. Nuc. Sci. NS-3220, 3144 (1985).

20. B. B. Godfrey and T. P. Hughes, Phys. Fluids 28, 669 (1985), and references therein.

21. R. J. Briggs, "Suppression of Transverse Beam Breakup Modes in an Induction Accelerator by Gas Focusing," UCID-18633 (Lawrence Livermore National Laboratory, 1980).

22. G. Caporaso, et. al., in Proc. 1985 SDIO/DARPA/Services Propagation Review, to be published (Secret).

23. B. B. Godfrey and T. P. Hughes, IEEE Trans. Nuc. Sci. NS-30, 2531 (1983).

24. E. P. Lee, A. Faltens, L. J. Laslett, and L. Smith, IEEE Trans. Nuc. Sci. NS-30, 2504 (1983).

25. F. Mako, W. Manheimer, C. A. Kapetanakos, D. Chernin, and F. Sandel, Phys. Fluids 27, 1815 (1984).

26. W. W. Rienstra and M. L. Sloan, "Recirculating Accelerator Magnet Design," (Science Applications International Corporation, Albuquerque 1985).

27. B. Hui and Y. Y. Lau, Phys. Rev. Lett. 53, 2024 (1984).

28. D. L. Book, NRL Plasma Formulary, (Naval Research Laboratory, Washington, 198), p. 30.

29. R. J. Adler, G. F. Kiuttu, B. E. Simpkins, D. J. Sullivan and D. E. Voss, "Improved Electron Emission by Use of a Cloth Fiber Cathode," (Mission Research Corporation, AMRC-N-275, October 1984).

30. P. M. Morse and H. Feshback, Methods of Mathematical Physics, (McGraw-Hill, New York, 1953), pp. 655-666.

31. J. A. Stratton, Electromagnetic Theory, (McGraw-Hill, New York, 1941), pp. 47-50.

32. B. B. Godfrey, " A Galerkin Algorithm for Multi-dimensional Plasma Simulation Codes," LA-7687-MS (Los Alamos National Laboratory, Los Alamos, 1979).

33. H. L. Buchanan, "The ANTIGONE Spaced-Based Ballistic Missile Defense System (U)," AFWL-TR-84-68 (Air Force Weapons Laboratory, Albuquerque, 1985) (Secret).

34. This case was suggested by E. P. Lee, private communication (1985).

35. B. B. Godfrey, D. Mitrovich, and L. A. Wright, "Magnetic Erosion Calculations (U)," AMRC-R-551 (Mission Research Corporation, Albuquerque, 1985) (Secret).

APPENDIX A

IFR BEAM EROSION AND ENERGY FLOW

We have compiled and generalized the formulas for energy partitioning during electron beam IFR transport in metallic drift tubes. The expressions are valid for relativistic, paraxial beams with pulse lengths much longer than the drift tube diameter. In addition, electrons expelled from the channel are assumed to strike the drift tube promptly. This last requirement may well be violated for $\nu > 1/2$. Ion motion is not considered.

Energy distribution among various particle species and fields can be defined in terms of three integrals:

$$U_{bb} = \frac{1}{8\pi} \int E_b^2 \, dA \tag{1}$$

$$U_{bi} = -\frac{1}{8\pi} \int E_b E_i \, dA \tag{2}$$

$$U_{ii} = \frac{1}{8\pi} \int E_i^2 \, dA \tag{3}$$

E_b and E_i are the radial electric fields due to the beam electrons and channel ions, respectively. $B_b = E_b$ and $B_i = 0$, where B_b and B_i are the corresponding azimuthal magnetic fields. The beam velocity, approximately equal to the speed of light, is normalized to unity.

The beam head loses energy inductively at a rate $2U_{bi}$, causing beam front erosion at a rate

$$\left.\frac{dx}{dz}\right|_i = \frac{2U_{bi}}{\nu\gamma} \tag{4}$$

Most of the energy, an amount $2U_{bi} - U_{ii}$, is carried off by channel electrons flying radially to the wall. The remainder, U_{ii}, contributes to the field energy behind the beam head, $2(U_{bb} - U_{bi}) + U_{ii}$.

Since the Poynting flux associated with the fields behind the beam front is $2(U_{bb} - U_{bi})$, steady-state energy conservation indicates that the the energy (per unit length) in the body is reduced below the injection energy by the same amount. This energy loss is simply the spacecharge depression of the beam in the ion channel. On this basis, the spacecharge limit is given approximately by

$$2(U_{bb} - U_{bi}) = \nu(\gamma_0^{2/3} - 1)^{3/2} \tag{5}$$

Just after the beam tail passes, the bare ion channel has an associated field energy U_{ii} but zero particle energy and Poynting flux. By energy balance or direct calculation, the beam tail neither gains nor loses energy inductively. Likewise, a second beam pulse following closely behind the first suffers no inductive erosion. To the extent that enough time elapses between pulses that field energy is converted to ion energy, some erosion may occur in the second pulse, however. Figure 5 summarizes the energy distribution among particles and fields.

The integrals (1) - (3) have been evaluated in two cases. For beam and channel of equal radius a enclosed in a drift tube of radius R,

$$U_{bb} = \nu^2 \left[\frac{1}{4} + \ell n(R/a)\right] \tag{6}$$

$U_{bi} = fU_{bb}$, and $U_{bi} = f^2 U_{bb}$; f is the channel-to-beam line density ratio. Inserting these results into Equation 4 gives the expected linear dependence of erosion on f.[33]

Suppose, instead, that the beam and IFR channel are surrounded by a low density background plasma within the drift tube.[34] Electrostatic fields near the beam head expel the plasma electrons within a radius b,

$$N_p b^2 = N_b a^2 (1 - f) \tag{7}$$

where N_p and N_b are the beam and plasma electron densities. The time required for expulsion is of order $b/(2\nu)^{1/2}$. We assume $b < R$. In this case,

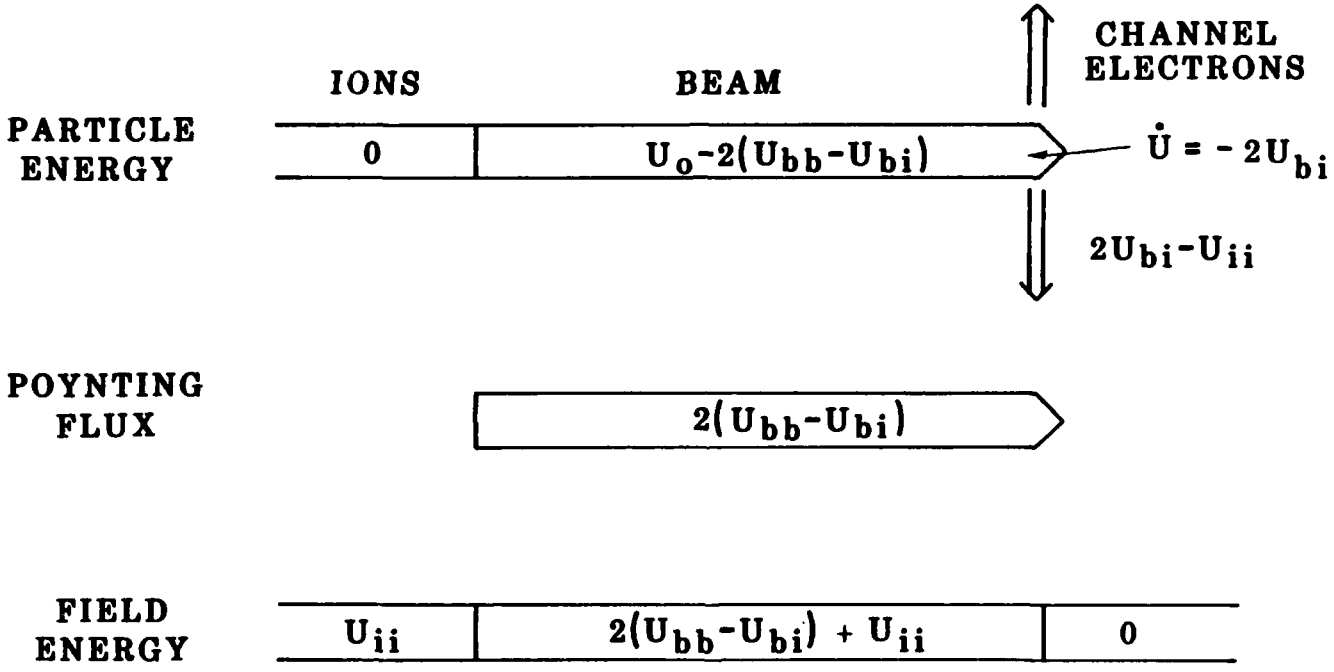

Figure 5. IFR beam transport energy partition diagram.

$$U_{bi} \approx \nu^2\left(\frac{2 - f}{4} + f\ \ell n\ b/a + \ell n\ R/b\right) \tag{8}$$

$$U_{ii} \approx \nu^2\left(\frac{1 + 2f - f^2}{4} + f^2\ \ell n\ b/a + \ell n\ R/b\right) \tag{9}$$

Erosion persists even in the limit of vanishing f. Note that this analysis does not allow for plasma return current flow at large radii.

Incidentally, when magnetic erosion[33,35] (or any erosion scaling as $\eta^{-1/2}$) occurs simultaneously with inductive erosion, it is easy to show that the combined erosion rate is approximately

$$\frac{dx}{dz} = \frac{1}{2}\frac{dx}{dz}\bigg|_i + \left\{\left[\frac{1}{2}\frac{dx}{dz}\bigg|_i\right]^2 + \left[\frac{dx}{dz}\bigg|_m\right]^2\right\}^{1/2} \tag{10}$$